Materials Science & Engineering A 769 (2020) 138526

Contents lists available at ScienceDirect

Materials Science & Engineering A

journal homepage: http://www.elsevier.com/locate/msea

Evolution of Guinier-Preston zones in cold-rolled $Al_{0.2}CoCrFeNi$ high-entropy alloy studied by synchrotron small-angle X-ray scattering

Yung-Chien Huang [a], Cheng-Si Tsao [b], Chieh Lin [a], Yi-Cheng Lai [a], Shyi-Kaan Wu [a,c,*], Chih-Hsuan Chen [c]

[a] Dept. of Materials Science and Engineering, National Taiwan University, Taipei, 106, Taiwan
[b] Nuclear Fuel and Materials Division, Institute of Nuclear Energy Research, Taoyuan, 325, Taiwan
[c] Dept. of Mechanical Engineering, National Taiwan University, Taipei, 106, Taiwan

ARTICLE INFO

Keywords:
High-entropy alloys
Small-angle X-ray scattering
Guinier-Preston zone
Precipitation hardening
Mechanical properties

ABSTRACT

The synchrotron small-angle X-ray scattering (SAXS) technique was used to investigate the morphological evolution of Guinier-Preston (GP) zones in 80% cold-rolled $Al_{0.2}CoCrFeNi$ high-entropy alloy aged at 550 °C for different times. The hardness profile exhibited double-peaked aging behavior. HRTEM observations revealed the appearance of the GP zones in specimens aged for two peak aging times. The SAXS analysis demonstrated that, according to their evolutions of relative volume fraction and size, the two groups of GP zones could be divided into GP1 and GP2 zones from 1 h of aging. The corresponding peaks in volume fraction and in size of GP1 and GP2 zones were correlated to the first and the second peak aging, respectively, indicating precipitation hardening by GP1 and GP2 zones. In addition, mechanical properties measured by tensile tests showed a trend similar to that of the hardness variation. The increasingly large particles after 1 h of aging detected by SAXS were also observed by TEM in 100 h over-aged specimens and identified as an AlNi-rich $L1_2$ phase. Based on the combined investigations of SAXS and TEM, the precipitation sequence in 80% cold-rolled $Al_{0.2}CoCrFeNi$ alloy aged at 550 °C is GP1 → GP2 → $L1_2$.

1. Introduction

High entropy alloys (HEAs) have attracted great interest in the last decade because their various composition systems exhibit novel mechanical and physical properties [1–8]. The vastness of the composition space containing at least several principal elements in approximately equiatomic ratios releases the restriction on the conventional approach of alloy design. Although many recent studies have indicated that secondary phases or precipitates (ppts) appear in most HEAs, which has led to the introduction of terms including multi-principal-element alloys (MPEAs) and complex concentrated alloys (CCAs), single-phase solid solutions are still attracting great attention, especially the FCC-structured HEAs [8–12]. One famous HEA with the FCC structure is the equiatomic CoCrFeMnNi alloy, which is well known due to its excellent mechanical properties and was first reported by Cantor et al. [2].

Another extensively studied alloy system is the $Al_xCoCrFeNi$ HEA, which has attracted much attention due to its phase variation and precipitation hardening effect [13–22]. The $Al_xCoCrFeNi$ alloy exhibits a single FCC phase with $x \leq 0.4$, a FCC + BCC dual-phase with $0.4 < x < 0.9$, and a single BCC structure with $x \geq 0.9$ [17,21,23]. When the volume fraction of the BCC phase is increased by increasing the Al content, the alloy possesses higher hardness and strength but lower ductility due to the brittle BCC phase [17,21]. The addition of Al into the alloy also enhances the formation of ppts during thermomechanical treatment, further increasing the hardness and strength of the alloy [13]. Tang et al. demonstrated that a combination of high-pressure torsion processing and thermal annealing could strengthen $Al_{0.3}CoCrFeNi$ HEA due to the precipitation of AlNi-rich B2-structured ppts [18]. Gwalani et al. also revealed the precipitations of ordered $L1_2$ ppts with a stoichiometric composition of $(Ni,Cr)_3(Al,Fe,Co)$ and B2 ppts in $Al_{0.3}CoCrFeNi$ HEA annealed at 550 °C and 700 °C, respectively [14]. The phase stability and the hardening effect of these ppts have been investigated by conventional microstructure analysis via TEM observations. In addition, the dislocation network caused by cold-rolling is reported to stimulate the precipitation in CoCrFeMnNi HEA during aging, which enhances the

* Corresponding author. Dept. of Materials Science and Engineering, National Taiwan University, Taipei, 106, Taiwan.
E-mail address: skw@ntu.edu.tw (S.-K. Wu).

https://doi.org/10.1016/j.msea.2019.138526
Received 13 August 2019; Received in revised form 3 October 2019; Accepted 8 October 2019
Available online 9 October 2019
0921-5093/© 2019 Elsevier B.V. All rights reserved.

nucleation of the ppts [11]. However, the formation and the evolution of the ppts in cold-rolled $Al_xCoCrFeNi$ alloy in the early aging period are less understood, and it is important to reveal the effect of the cold-rolling on age precipitation and the relationship between the ppts and mechanical properties.

In this study, to prevent the brittle BCC phase from the deterioration of the mechanical properties, $Al_{0.2}CoCrFeNi$ alloy with a single-phase FCC-structure was investigated with the small-angle X-ray scattering (SAXS) technique using high-energy synchrotron radiation. The SAXS technique is an effective approach to quantitatively determine the morphological evolution and kinetic behavior of a great number of nanoscale precipitates in a bulk alloy sample. In the present study, the SAXS analysis revealed the temporal evolution and growth kinetics of Guinier-Preston (GP) zones in 80% cold-rolled $Al_{0.2}CoCrFeNi$ alloy aged at 550 °C in terms of the radius, the thickness and the relative volume fraction, which are also correlated with the mechanical properties of the alloy.

2. Experimental procedures

An alloy ingot with a nominal composition of $Al_{0.2}CoCrFeNi$ in atomic ratio was prepared by arc melting in high-purity argon atmosphere with a mixture of raw metals. The purity of each metal was higher than 99.9 wt%. The ingot was flipped and remelted six times to improve the homogeneity of the composition. The ingot was then homogenized at 1100 °C for 24 h in a tube furnace with an argon flow. The homogenized ingot was subsequently cold-rolled at room temperature into a plate with thickness reduction of 80%. The specimens for the following measurements and tests were cut from the plate to appropriate sizes and ground to the optimal thickness, aged at 550 °C for different times, and quenched in water.

The SAXS measurements were conducted at the BL23A beamline, National Synchrotron Radiation Research Center (NSRRC), Taiwan, with high-flux collimated X-rays of 15 keV and a beam size of ~500 μm. The SAXS specimens were ground to a thickness of ~20 μm at the detected area for optimal transmission. According to standard procedures of data reduction, calibration, and background correction, each 2D SAXS pattern was azimuthally averaged into a 1D SAXS profile as a function of the scattering vector $Q = 4\pi\sin(\theta/2)/\lambda$, in which θ is the scattering angle and λ is the X-ray wavelength. The microstructure was also examined using a transmission electron microscope (TEM, Philips Tecnai^{TM} G^2 F20). The TEM specimens were ground to ~70 μm in thickness and punched into disks with a diameter of 3 mm. Thereafter, the disks were twin-jet polished at about −40 °C in electrolyte of 20% nitric acid and 80% methanol (in vol.). The Vickers microhardness was measured with a hardness tester (Mitutoyo HM, Japan) with an applied load of 300 g and a loading time of 15 s. The hardness values were averaged from at least eight data for each specimen aged for different times. The tensile tests were conducted with a tensile testing machine (AG-IS, Shimadzu, Japan) with a maximum loading of 50 kN. The dog-bone specimens had a gauge length of 17 mm, a width of 6 mm, and a thickness of 1.6 mm. The tests were performed at room temperature with a strain rate of 1×10^{-4} s^{-1}.

3. Results

3.1. Hardness variation

Fig. 1 shows the hardness evolution of the cold-rolled $Al_{0.2}CoCrFeNi$ alloy aged at 550 °C for different times from as the cold-rolled state to 100 h of aging. In Fig. 1, the curve of the hardness profiles displays two hardening peaks that occurred respectively at the aging times of 15 min and 25 h, indicating a complex variation in the microstructure of the alloy. The as cold-rolled alloy exhibited hardness of 410 HV, which is much higher than that of the recrystallized alloy with a quite similar composition of $Al_{0.3}CoCrFeNi$, which is 140–200 HV, depending on grain size, due to the strain hardening by cold-rolling [13]. When the specimen was aged at 550 °C, the hardness increased significantly in 5 min to 471 HV, an increment of 61 HV. The first peak occurred at the aging time of 15 min, when the hardness reached 473 HV. Then the value of the hardness dropped to 451 HV at 1 h of aging. With further aging, the second hardening peak exhibited a hardness value of 486 HV at 25 h of aging, which is even higher than that of the first hardening peak.

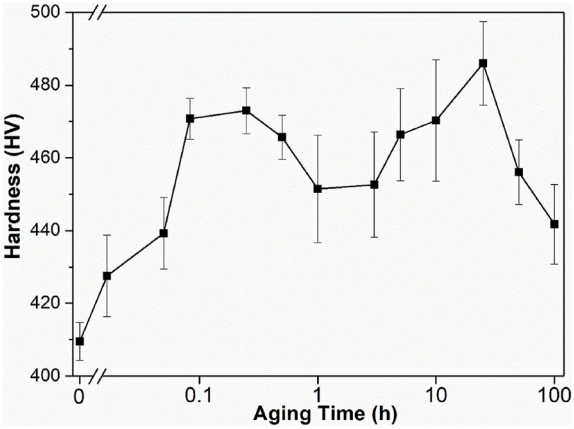

Fig. 1. Evolution of the measured hardness of the cold-rolled $Al_{0.2}CoCrFeNi$ alloy aged at 550 °C for different times.

3.2. Microstructure observation

For the purpose of realizing the microstructure of the $Al_{0.2}CoCrFeNi$ alloy in the two peak aging states and in the softening state, TEM observations were performed on as cold-rolled specimens aged at 550 °C for 15 min, 1 h and 25 h. Fig. 2(a), 2(b) and 2(c) present high-resolution TEM (HRTEM) images of the microstructures corresponding to 15 min, 1 h and 25 h of aging, respectively. The insets in Fig. 2(a)-(c) demonstrate the corresponding fast Fourier transform (FFT) patterns. The

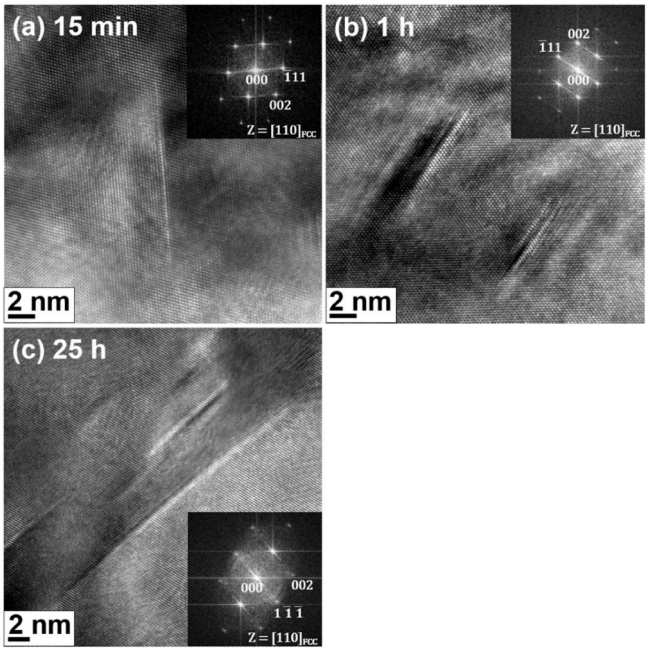

Fig. 2. HRTEM images of the cold-rolled $Al_{0.2}CoCrFeNi$ alloy aged at 550 °C for (a) 15 min, (b) 1 h and (c) 25 h. The inset in each image is the corresponding fast Fourier transform (FFT) pattern.

HRTEM micrographs were all obtained from the 110_{FCC} zone. As can be seen in Fig. 2(a), plate-shaped ppts were found in the matrix; they were related to the first hardening peak at 15 min. Such ppts are regarded as GP zones in other alloy systems [24], and therefore the plate-shaped ppts are also referred to as GP zones in this study. The GP zones were about 10 nm in length and about 1 nm in thickness. When the specimen was further aged to 1 h, as shown in Fig. 2(b), the GP zones seemed to shrink in length to less than 10 nm and to slightly thicken. In the specimen aged for 25 h, the GP zones also existed in the alloy, as shown in Fig. 2(c). As compared to the GP zones in the 15 min-aged state, the GP zones in the 25 h-aged specimen were about 20 nm in length and had a nearly constant thickness of around 1 nm. The averaged size was measured from at least five GP zones in the HRTEM images for each specimen aged for different aging times. From the FFT patterns shown in Fig. 2(a)-(c), the ppts of GP zones were determined to lie on the $\{111\}_{FCC}$ planes of the FCC matrix. Note that it would have been insufficient to clarify whether the GP zones in the 15 min-, 1 h- and 25 h-aged specimens were the same kind of ppts from only the differences in the size determined by TEM technique, so further investigation was needed to reveal the evolutions of the GP zones.

3.3. Small-angle X-ray scattering (SAXS) analysis

Due to the limitations of the TEM observations, which can only detect a localized nanometric scale scope and hence cannot provide a comprehensive view, the SAXS technique was employed as a complementary method to measure a considerable region with an area of hundreds of micrometers in a quantitative and statistical manner. In this study, the SAXS was conducted on cold-rolled $Al_{0.2}CoCrFeNi$ specimens aged at 550 °C for different times. Fig. 3(a)-(d) show the representative 2D SAXS patterns of specimens aged for 0 min, 15 min, 1 h and 25 h, which were in the as cold-rolled, first peak aging, hardness dip and second peak aging states, respectively. As can be seen in Fig. 3, the SAXS patterns of all specimens revealed radial streaks, which evidenced the appearance of the plate-like ppts, showing consistence with the shape of the GP zones observed by HRTEM. It is worth noting that the GP zones formed in the as cold-rolled specimens without any aging. With increasing aging time, the isotropic scattering intensities around the center increased slightly in the first 1 h of aging, and a significant increase emerged at 25 h of aging, indicating that large particles formed and grew during 1 h–25 h of aging. To further quantitatively analyze the morphological evolution of the GP zones, the 2D SAXS patterns were reduced to 1D SAXS profiles by azimuthal average method. Fig. 4(a) and (b), and 4(c) show the 1D SAXS profiles of the $Al_{0.2}CoCrFeNi$ HEA aged at 550 °C for the aging times of 0 min–15 min, 15 min to 1 h, and 1 h–25 h, corresponding to the first hardening, the softening, and the second hardening of the hardness profile in Fig. 1, respectively.

As shown in Fig. 4(a) and (b), for the specimens in the first 1 h of aging, the upturn of intensities in the low Q region (0.007 $Å^{-1}$–0.02 $Å^{-1}$) remained almost constant and exhibited the power-law scattering behavior, $I(Q) \propto Q^{-4}$, resulting from the large particles, which may have arisen from the small amounts of the inevitable oxides or impurities during the ingot preparation. Since the GP zones exhibited a plate-like morphology, as resolved from the HRTEM observations and the 2D SAXS patterns, the radius, thickness and relative volume fraction of the GP zones can be quantitatively modeled by Eq. (1).

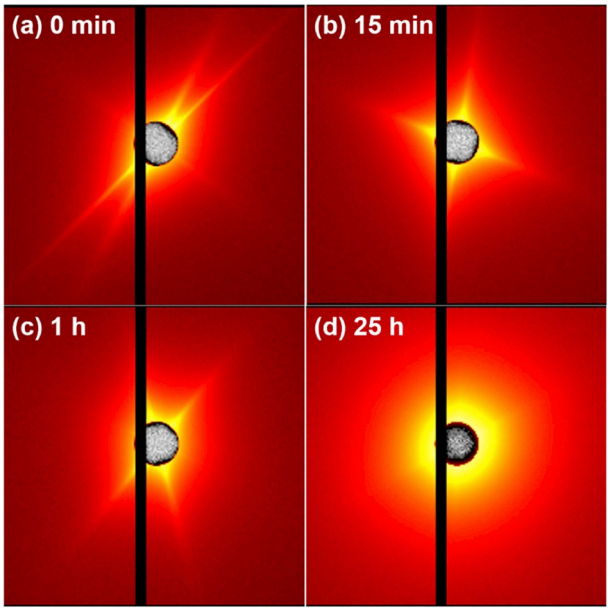

Fig. 3. Evolution of 2D SAXS patterns of the cold-rolled $Al_{0.2}CoCrFeNi$ alloy aged at 550 °C for (a) 0 min, (b) 15 min, (c) 1 h and (d) 25 h.

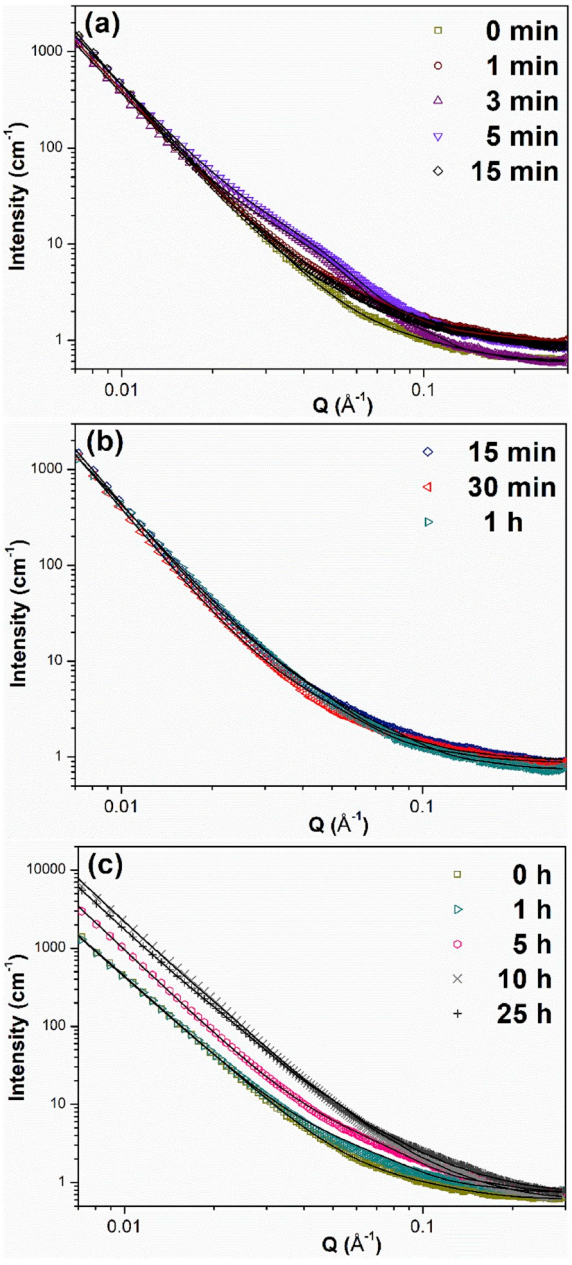

Fig. 4. Evolution of 1D SAXS profiles of the cold-rolled $Al_{0.2}CoCrFeNi$ alloy aged at 550 °C for (a) 0min–15min, (b) 15min–1h and (c) 0min–25 h. (The solid fitted curves represent the intensities calculated by SAXS models.)

$$I(Q) = AQ^{-4} + I_{\text{plate}}(Q) + b \quad (1)$$

where the first term describes the surface scattering resulting from the large particles and A is a constant. The constant b is incoherent background scattering. The second term, $I_{plate}(Q)$, is the form factor of the plate-like GP zones, as expressed by Eq. (2) [25–29].

$$I_{\text{plate}}(Q) = \frac{\eta}{V_p} \cdot \Delta\rho^2 \cdot \int_0^{\frac{\pi}{2}} \left[2(\pi R^2 T) j_0\left(\frac{QT}{2}\cos\theta\right) \frac{j_1(QR\sin\theta)}{(QR\sin\theta)} \right]^2 (\sin\theta) d\theta \quad (2)$$

where η is the volume fraction of GP zones in the specimen, $\Delta\rho$ denotes the scattering length density contrast between the GP zones and the matrix, and j_0 and j_1 are the zero-order and first-order Bessel functions, respectively. V_p is the particle volume. The integral over θ averages the form factor over all possible orientations of the disks with a solid angle θ with respect to Q. The product of η and $\Delta\rho^2$ can be regarded as a pre-factor constant. Thus, the relative volume fraction η can be obtained by the relative pre-factor by assuming that the $\Delta\rho^2$ value is fixed via model fitting.

For the further aging to 25 h, as shown in Fig. 4(c), the intensity upturn in the low Q region (0.007 $Å^{-1}$–0.04 $Å^{-1}$) increased remarkably when the specimens were aged for more than 1 h. The SAXS profile of the as cold-rolled state is also presented in Fig. 4(c) for comparison. The increasing intensities in the low Q region signified that a phase of large size formed and grew with increasing aging time. In addition to the growing large particles, the intensities in the middle Q region (0.08 $Å^{-1}$–0.2 $Å^{-1}$) also exhibited a gradual increment with increasing aging time. The turning point at the Q of 0.08 $Å^{-1}$ resulted in a flatter slope in the middle Q region, which differed from the power-law scattering behavior in the low Q region, indicating bimodal precipitation during the aging after 1 h. Therefore, the SAXS profiles of 5 h, 10 h and 25 h were fitted using the sum of intensities contributed by both growing large particles and GP zones as shown in Eq. (3).

$$I(Q) = I_{\text{large}}(Q) + I_{\text{plate}}(Q) + b \quad (3)$$

Here, the large particles are supposed to be sphere-shaped due to the isotropic scattering near the center in the 2D SAXS pattern for the specimen aged for 25 h, as shown in Fig. 3(d). The SAXS intensity caused by the large particles can be modeled by Eq. (4) [25,27–29].

$$I_{\text{large}}(Q) = A \cdot \int_0^{\infty} g(R) \left[\frac{\sin(QR) - QR\cos(QR)}{(QR)^3} \right]^2 dR \quad (4)$$

where the constant A is a pre-factor. The large ppts have the Schulz distribution $g(R)$ in particle radius R. All the SAXS profiles in Fig. 4 corresponding to the different aging periods of the specimens aged at 550 °C fit well using Eq. (1) and Eq. (3). However, due to the limitation of SAXS measurement in this study, the volume fraction and the size of the large particles could not be accurately estimated, and only the evolution of the GP zones was resolved.

Determined by model fitting analysis for the $Al_{0.2}$CoCrFeNi alloy aged at 550 °C, the temporal evolution of the relative volume fraction of the GP zones normalized by the maximum value is shown in Fig. 5. In that figure, the curve of the relative volume fraction increases to the first peak at 15 min of aging and then decreases to the dip at 1 h of aging, followed by the second ascent. This growth behavior of double-peaked aging can be presumed to result from two GP zones that divided from 1 h of aging. Therefore, in this study, the first peak was caused by the GP zones denoted as GP1, while the second peak was caused by those denoted as GP2. Meanwhile, the evolutions of the radius and thickness of the GP1 and GP2 zones analyzed by the model fitting are also demonstrated in Fig. 6(a) and (b), respectively. The length and thickness of the GP zones measured from HRTEM images are also marked in Fig. 6 (a) and (b) for comparison. Combining the morphological evolutions of the GP1 and GP2 zones in Figs. 5 and 6, the curves of the radius and the relative volume fraction exhibited a similar trend of double-peaked

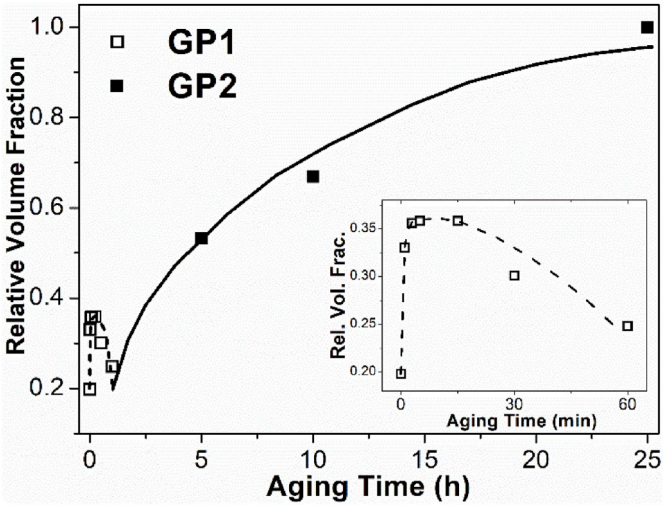

Fig. 5. Evolution of the relative volume fraction of the GP1 and GP2 in the cold-rolled $Al_{0.2}$CoCrFeNi alloy aged at 550 °C.

behavior, while the thickness remained nearly constant at ~1 nm. Although the GP zones before and after 1 h of aging are called GP1 and GP2, respectively, it is still unknown whether the GP2 evolved from the GP1 or was a newly-nucleated precipitate. The distinction between GP1 and GP2 merely comes from the presence of two kinetic stages of precipitation. Therefore, further investigation is needed.

3.4. Mechanical properties

Fig. 7 shows the measured stress-strain (σ-ε) curves of the cold-rolled $Al_{0.2}$CoCrFeNi HEA aged at 550 °C for the aging times of 0 min, 15 min, 1 h, 25 h and 100 h. Based on Fig. 7, the 0.2% offset yield strength (σ_y), ultimate tensile strength (σ_u) and elongation (ε) of the specimens are listed in Table 1. As shown in that table, the as cold-rolled specimen had high σ_y of 1094 MPa with moderate ductility of 9.6%. Increasing the aging time to 15 min increased the σ_y and σ_u significantly to 1439 MPa and 1541 MPa, respectively. With further aging to 1 h, all these mechanical properties dropped slightly, to 1312 MPa for σ_y and 1404 MPa for σ_u. At the aging time of 25 h, the values of the σ_y and σ_u reached their maximum of 1443 MPa and 1544 MPa, respectively. When the specimen was aged for a longer time of 100 h, which was an over-aged state, the values of σ_y and σ_u decreased to 1191 MPa and 1319 MPa, respectively. It was found that the strength variation in terms of the σ_y and σ_u had two maximum values at the corresponding peak aging times, based on the Vickers microhardness profile plotted in Fig. 1. However, while the strength exhibited a similar trend with the hardness during the 550 °C aging, the elongation decreased with increases in aging time in the first 25 h but significantly increased with further aging of 100 h.

4. Discussion

4.1. Effect of cold-rolling on the precipitation behavior

FCC-structured Al_xCoCrFeNi HEAs with $x < 0.4$ have been investigated to determine the precipitation behaviors with different grain sizes and aging temperatures [13–16,18,19]. It is reported that in the $Al_{0.3}$CoCrFeNi alloy, $L1_2$ ppts form at a medium aging temperature of 500–550 °C and the B2 ppts form at a higher aging temperature of ~700 °C [14,18]. However, the precipitation of the FCC-structured Al_xCoCrFeNi HEAs in the early aging stage with the facilitation of the dislocations had yet to be investigated. In this study, Fig. 1 demonstrates the double-peaked aging in the cold-rolled $Al_{0.2}$CoCrFeNi alloy aged at 550 °C. Although there might be some recovery or recrystallization during aging which would cause the hardness decrease between the two

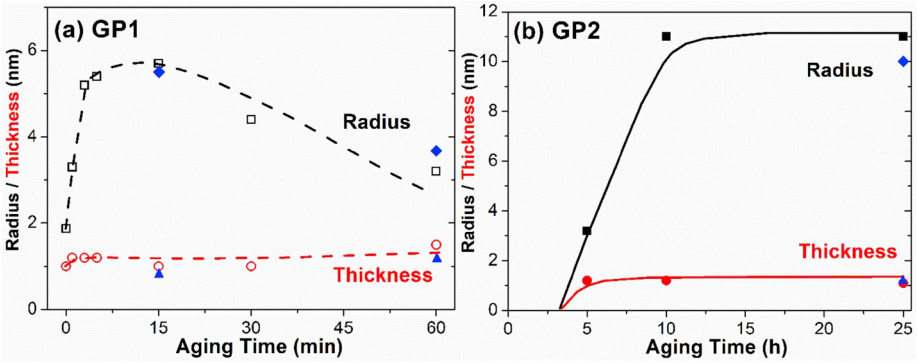

Fig. 6. Evolutions of the radii and thicknesses for the (a) GP1 and (b) GP2 in the cold-rolled $Al_{0.2}CoCrFeNi$ alloy aged at 550 °C. The radius (diamond) and thickness (triangle) measured from HRTEM images of Fig. 2 are also marked as blue points for comparison. (For interpretation of the references to colour in this figure legend, the reader is referred to the Web version of this article.)

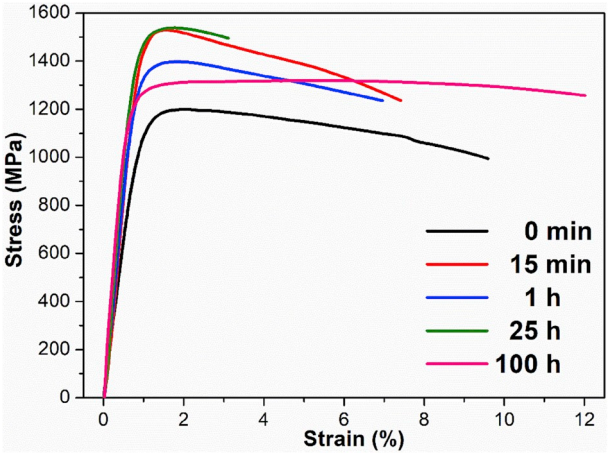

Fig. 7. The stress-strain (σ-ε) curves of the cold-rolled $Al_{0.2}CoCrFeNi$ alloy aged at 550 °C for 0 min, 15 min, 1 h, 25 h and 100 h with a strain rate of 1×10^{-4} s^{-1}.

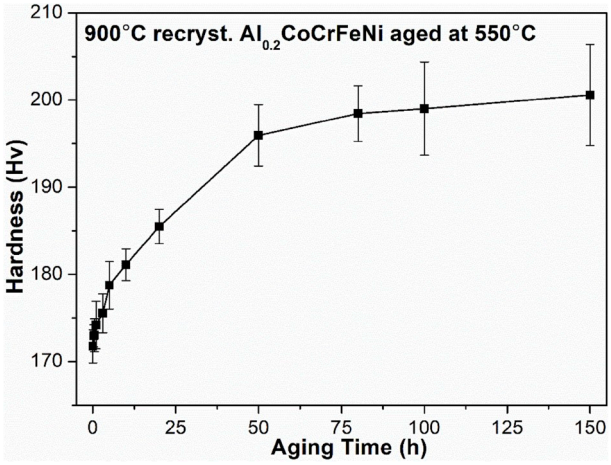

Fig. 8. Evolution of the measured hardness during 550 °C aging in the 80% cold-rolled $Al_{0.2}CoCrFeNi$ alloy recrystallized at 900 °C followed by water-quenching.

Table 1
The corresponding results of tensile tests for the cold-rolled $Al_{0.2}CoCrFeNi$ alloy aged at 550 °C for 0 min, 15 min, 1 h, 25 h and 100 h.

State	0 min	15 min	1 h	25 h	100 h
Yield Stress, 0.2% offset, σ_y (MPa)	1094	1439	1312	1443	1191
Ultimate Tensile Stress, σ_u (MPa)	1205	1541	1404	1544	1319
Elongation, ε (%)	9.6	7.2	6.9	3.1	12.0

peaks, the significant increase in the hardness from 410 HV to 471 HV within 5 min indicated that the softening by recovery or recrystallization could be neglected compared to that affected by the evolution of the GP zones. The SAXS analysis also resolved that the first and the second hardening effects may come from GP1 and GP2 zones, respectively, as shown in Figs. 5 and 6. To compare the effect of cold-rolling on precipitation behavior, the hardness evolution during 550 °C aging of 80% cold-rolled $Al_{0.2}CoCrFeNi$ alloy recrystallized at 900 °C and water-quenched is plotted in Fig. 8. As shown in Fig. 8, the value of hardness increases continuously in the first 50 h of 550 °C aging and then saturates until 150 h, indicating no double-peaked aging behavior. Previous studies have pointed out that the ppts that form during 550 °C aging are the $L1_2$ phase [13,14]. Therefore, the difference in the alloy with or without cold-rolling, which can or cannot introduce dislocations, results in two different precipitation hardening profiles. The introduction of a dislocation network has been investigated in a CoCrFeMnNi alloy, and such a network can enhance the formation of the homogeneously dispersed nanoprecipitates [11,30]. The dislocations are supposed to act as the nucleation sites of the ppts. Comparing the hardness values in the 80% cold-rolled state and in the recrystallized state of the $Al_{0.2}CoCrFeNi$ alloy in Figs. 1 and 8, respectively, the hardness in the cold-rolled state increases drastically within only 15 min of aging and reaches an even higher value at 25 h of aging due to the formation of GP zones, while that in the recrystallized state gives a smaller increment in hardness value and needs a longer aging time of 50 h to saturation.

4.2. *Correlation between the morphological evolution of the GP zones and the mechanical properties*

The combined investigations of SAXS, HRTEM and mechanical tests are presented for a quantitative analysis of the morphological evolution of the GP zones corresponding to the mechanical properties. Figs. 5 and 6 demonstrate that the double hardness peaks in Fig. 1 are mainly contributed by GP1 and GP2, respectively. GP1 exists in the as cold-rolled specimen and grows during 550 °C aging. The increasing volume fraction of GP1 in the first 15 min of aging leads to the increase in the hardness. When the GP1 starts to dissolve and is transferred to GP2 after 15 min, the size and the volume fraction of the GP1 drop, according to Figs. 5 and 6, which reflect the softening of the alloy in Fig. 1. For the second ascent of the hardness, not only the GP2 but also the large particles increase in volume fraction with increasing aging time.

Although these growing large particles have been detected by SAXS,

as shown in Fig. 4(c), they are still difficult to observe by TEM when they have just formed in their early stage. Therefore, the specimen aged for a longer time of 100 h was observed with TEM to clarify the structure and the composition of the large particles when the ppts are of sufficient size and amount. Fig. 9(a) is the TEM selected area electron diffraction pattern (SADP) of the specimen aged at 550 °C for 100 h, indicating the appearance of $L1_2$ particles in the FCC matrix. The corresponding dark-field image, obtained from the $(1\bar{1}0)$ $L1_2$ superlattice reflection marked by a circle in Fig. 9(a), is revealed in Fig. 9(b). The composition of the $L1_2$ particle was also detected by energy dispersive spectroscopy (EDS) in the TEM and is revealed in the inset of Fig. 9(b), indicating that the particle was an AlNi-rich phase. Although the composition of the nano-scale particles was smeared by the matrix during EDS measurement, it still provided an approximate composition of the ppts for reference. The precipitation hardening of these AlNi-rich $L1_2$-structured particles has been intensively studied, for they also act as the main hardening phase in the recrystallized $Al_{0.2}$CoCrFeNi alloy shown in Fig. 8 [13,18]. Therefore, based on the hardness profile in Fig. 1, the contribution to the hardening during the aging from 1 h to 25 h may come from the coexistence of both GP2 and $L1_2$ ppts. However, despite the fact that the $L1_2$ ppts contribute to the precipitation hardening, the GP2 still takes up the dominant hardening phase at 25 h peak aging because the $L1_2$ ppts could only give rise to a hardness increment of ~30 HV, relative to the original state, in the specimen aged for 100 h, as revealed in Fig. 8. Meanwhile, as shown in Fig. 7 and Table 1, the evolutions of σ_y and σ_u of the specimens in the as cold-rolled, first peak aging, softening dip, second peak aging and over-aging states, measured by tensile tests, also demonstrated a similar trend to the hardness curve shown in Fig. 1. Moreover, based on the mechanical properties in Fig. 7 and the morphological evolution of the GP zones in Figs. 5 and 6, the reduction of the elongation with increases in aging time in the first 25 h of aging may be attributed to the GP zones. Therefore, the specimen in the 100 h over-aged state exhibited the highest value of elongation among all the other specimens in different states, instead of further decreasing in elongation with increasing aging time, due to the very few GP zones in the 100 h-aged specimen. Double-peaked aging behaviors also occur in other alloy systems, such as Al–Cu alloy and Al–Zn–Mg alloy [31–37]. The precipitation sequences of GPI zone → GPII zone (θ'') → θ' → θ in Al–Cu alloy [31,32] and GP zone → η' → η in Al–Zn–Mg alloy [35,36] correlating to their double hardness peaks have been studied with various measurements and tests. In Al–Cu alloy [24], which has been well-investigated for several decades, the initial rise in hardness after the start of the aging is associated with the GPI zones. Then the maximum hardness of the alloy is attained when the amount of the θ'' ppts reaches its maximum. In addition, for the compensation of the strain field by defects, the formation of the θ'' ppts in Al–Cu alloy favors heterogeneous nucleation at defects, especially at dislocations, indicating a similar situation to that in this study, in which the development of the GP zones was stimulated by cold-rolling in $Al_{0.2}$CoCrFeNi alloy. However, the interrelations of these ppts in Al–Cu alloy have yet to be well understood. A few works from Silcock et al. deduced that the GPI zone, θ'', and θ' in Al–Cu alloy may be capable of independent nucleation [38]. In the present study, the 80% cold-rolled $Al_{0.2}$CoCrFeNi alloy was revealed to exhibit the precipitation sequence of GP1 → GP2 → $L1_2$ at 550 °C aging. The first and the second hardness peaks are correlated with the evolutions by the GP1 and GP2 ppts, respectively, with both having significant precipitation hardening effects. In the future, investigations of the relationship between these two ppts and of the optimal control of these ppts to enhance the mechanical properties for possible applications will need to be conducted.

5. Conclusions

The 80% cold-rolled $Al_{0.2}$CoCrFeNi high-entropy alloy aged at 550 °C has been investigated by synchrotron SAXS technique, HRTEM observations and mechanical property tests. The previous TEM investigations demonstrated that the recrystallized $Al_{0.3}$CoCrFeNi alloys aged at 550 °C would form the spherical nano-scale $L1_2$ precipitates which caused the precipitation hardening. In this study, the $Al_{0.2}$CoCrFeNi alloy was first cold-rolled with considerable thickness reduction, followed by the precipitation aging treatment. The dislocations and texture induced by cold-rolling modified the precipitation behavior of the alloy. The dislocation networks facilitated the faster precipitation to peak aging and even more increase in the hardness and the strength. Furthermore, the double peak aging effect appeared in the early aging, which was analyzed by SAXS measurements and HRTEM observations. According to the morphological evolution of the precipitates, it was proposed that the two hardness peaks resulted from the GP zones which were further denominated as GP1 and GP2 correlated to the first and the second peaks, respectively. The increasing $L1_2$ phase was also detected during the period of the second hardening. Therefore, the precipitation sequence in the cold-rolled $Al_{0.2}$CoCrFeNi alloy aged at 550 °C was revealed to be GP1 → GP2 → $L1_2$. However, the denomination of GP1 and GP2 was just used to demonstrate the two stages of precipitation. The relationship between GP1 and GP2 has yet to be clarified and needs to be further investigated. The induction of the dislocation networks provides the nucleation sites for the precipitates, shortens the peak aging time, and results in significant increase in the strength of the alloy, which can reduce the processing time and suggest a possible way to enhance the mechanical properties for structural applications.

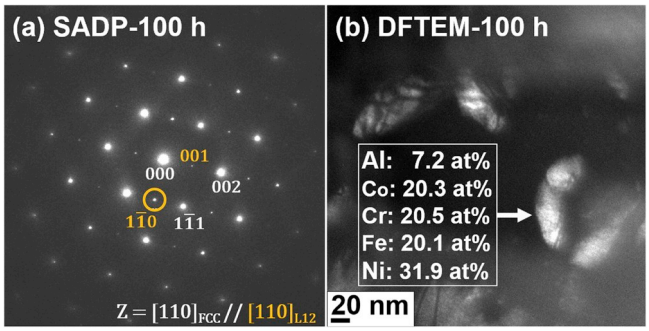

Fig. 9. (a) TEM selected are electron diffraction pattern (SADP) from $[110]_{FCC}//[110]_{L12}$ zone axis and (b) dark-field TEM (DFTEM) image, obtained from $(1\bar{1}0)$ superlattice reflection as marked by circle in Fig. 9(a), in the cold-rolled $Al_{0.2}$CoCrFeNi alloy aged at 550 °C for 100 h, showing the appearance of the $L1_2$ precipitates. The composition of the L12 precipitate measured by EDS in TEM is revealed in the inset of Fig. 9(b).

Declaration of competing interest

The authors declare that they have no known competing financial interests or personal relationships that could have appeared to influence the work reported in this paper.

Acknowledgements

The authors gratefully acknowledge the financial support for this study provided by the Ministry of Science and Technology (MOST), Taiwan, under Grants MOST 107-2218-E002-019 and MOST 107-2221-E002-016-MY2.

References

[1] J.W. Yeh, S.K. Chen, S.J. Lin, J.Y. Gan, T.S. Chin, T.T. Shun, C.H. Tsau, S.Y. Chang, Nanostructured high-entropy alloys with multiple principal elements: novel alloy design concepts and outcomes, Adv. Eng. Mater. 6 (2004) 299–303.
[2] B. Cantor, I.T.H. Chang, P. Knight, A.J.B. Vincent, Microstructural development in equiatomic multicomponent alloys, Mater. Sci. Eng. A 375 (2004) 213–218.
[3] J.W. Yeh, Recent progress in high-entropy alloys, Ann. Chim. Sci. Mater. 31 (2006) 633–648.

[4] J.W. Yeh, Physical metallurgy of high-entropy alloys, JOM (J. Occup. Med.) 67 (2015) 2254–2261.
[5] D.B. Miracle, J.D. Miller, O.N. Senkov, C. Woodward, M.D. Uchic, J. Tiley, Exploration and development of high entropy alloys for structural applications, Entropy 16 (2014) 494–525.
[6] M.H. Tsai, J.W. Yeh, High-entropy alloys: a critical review, Mater. Res. Lett. 2 (2014) 107–123.
[7] Y. Zhang, T.T. Zuo, Z. Tang, M.C. Gao, K.A. Dahmen, P.K. Liaw, Z.P. Lu, Microstructures and properties of high-entropy alloys, Prog. Mater. Sci. 61 (2014) 1–93.
[8] D.B. Miracle, O.N. Senkov, A critical review of high entropy alloys and related concepts, Acta Mater. 122 (2017) 448–511.
[9] E.J. Pickering, R. Munoz-Moreno, H.J. Stone, N.G. Jones, Precipitation in the equiatomic high-entropy alloy CrMnFeCoNi, Scr. Mater. 113 (2016) 106–109.
[10] J.Y. He, C. Zhu, D.Q. Zhou, W.H. Liu, T.G. Nieh, Z.P. Lu, Steady state flow of the FeCoNiCrMn high entropy alloy at elevated temperatures, Intermetallics 55 (2014) 9–14.
[11] W. Zhou, L.M. Fu, P. Liu, X.D. Xu, B. Chen, G.Z. Zhu, X.D. Wang, A.D. Shan, M. W. Chen, Deformation stimulated precipitation of a single-phase CoCrFeMnNi high entropy alloy, Intermetallics 85 (2017) 90–97.
[12] F. Otto, A. Dlouhy, K.G. Pradeep, M. Kubenova, D. Raabe, G. Eggeler, E.P. George, Decomposition of the single-phase high-entropy alloy CrMnFeCoNi after prolonged anneals at intermediate temperatures, Acta Mater. 112 (2016) 40–52.
[13] B. Gwalani, V. Soni, M. Lee, S.A. Mantri, Y. Ren, R. Banerjee, Optimizing the coupled effects of Hall-Petch and precipitation strengthening in a $Al_{0.3}$CoCrFeNi high entropy alloy, Mater. Des. 121 (2017) 254–260.
[14] B. Gwalani, V. Soni, D. Choudhuri, M. Lee, J.Y. Hwang, S.J. Nam, H. Ryu, S. H. Hong, R. Banerjee, Stability of ordered L1(2) and B-2 precipitates in face centered cubic based high entropy alloys - $Al_{0.3}$CoFeCrNi and $Al_{0.3}$CuFeCrNi$_2$, Scr. Mater. 123 (2016) 130–134.
[15] Z. Li, S. Zhao, H. Diao, P.K. Liaw, M.A. Meyers, High-velocity deformation of $Al_{0.3}$CoCrFeNi high-entropy alloy: remarkable resistance to shear failure, Sci. Rep. 7 (2017) 42742.
[16] D.Y. Li, C.X. Li, T. Feng, Y.D. Zhang, G. Sha, J.J. Lewandowski, P.K. Liaw, Y. Zhang, High-entropy $Al_{0.3}$CoCrFeNi alloy fibers with high tensile strength and ductility at ambient and cryogenic temperatures, Acta Mater. 123 (2017) 285–294.
[17] Y. Ma, B.B. Jiang, C.L. Li, Q. Wang, C. Dong, P.K. Liaw, F. Xu, L. Sun, The BCC/B2 morphologies in AlxNiCoFeCr high-entropy alloys, Metals 7 (2017) 57.
[18] Q.H. Tang, Y. Huang, Y.Y. Huang, X.Z. Liao, T.G. Langdon, P.Q. Dai, Hardening of an $Al_{0.3}$CoCrFeNi high entropy alloy via high-pressure torsion and thermal annealing, Mater. Lett. 151 (2015) 126–129.
[19] T.T. Shun, Y.C. Du, Microstructure and tensile behaviors of FCC $Al_{0.3}$CoCrFeNi high entropy alloy, J. Alloy. Comp. 479 (2009) 157–160.
[20] S.G. Ma, P.K. Liaw, M.C. Gao, J.W. Qiao, Z.H. Wang, Y. Zhang, Damping behavior of AlxCoCrFeNi high-entropy alloys by a dynamic mechanical analyzer, J. Alloy. Comp. 604 (2014) 331–339.
[21] W.R. Wang, W.L. Wang, S.C. Wang, Y.C. Tsai, C.H. Lai, J.W. Yeh, Effects of Al addition on the microstructure and mechanical property of AlxCoCrFeNi high-entropy alloys, Intermetallics 26 (2012) 44–51.
[22] L.L. Ma, L. Wang, Z.H. Nie, F.C. Wang, Y.F. Xue, J.L. Zhou, T.Q. Cao, Y.D. Wang, Y. Ren, Reversible deformation-induced martensitic transformation in $Al_{0.6}$CoCrFeNi high-entropy alloy investigated by in situ synchrotron based high-energy X-ray diffraction, Acta Mater. 128 (2017) 12–21.
[23] Y.F. Kao, T.J. Chen, S.K. Chen, J.W. Yeh, Microstructure and mechanical property of as-cast, -homogenized, and -deformed AlxCoCrFeNi (0 <= x <= 2) high-entropy alloys, J. Alloy. Comp. 488 (2009) 57–64.
[24] Reza Abbaschian, Lara Abbaschian, Robert E. Reed-Hill, Physical Metallurgy Principles, Cengage Learning Inc., Florence, KY, United States, 2009, pp. 507–509.
[25] O. Glatter, O. Kratky, Small Angle X-ray Scattering, Academic Press, 1982, p. 222.
[26] F. De Geuser, F. Bley, A. Deschamps, A new method for evaluating the size of plate-like precipitates by small-angle scattering, J. Appl. Crystallogr. 45 (2012) 1208–1218.
[27] A. Deschamps, F. De Geuser, On the validity of simple precipitate size measurements by small-angle scattering in metallic systems, J. Appl. Crystallogr. 44 (2011) 343–352.
[28] A. Deschamps, F. De Geuser, Quantitative characterization of precipitate microstructures in metallic alloys using small-angle scattering, Metall. Mater. Trans. A 44A (2013) 77–86.
[29] S.R. Kline, Reduction and analysis of SANS and USANS data using IGOR Pro, J. Appl. Crystallogr. 39 (2006) 895–900.
[30] Y.C. Huang, C.S. Tsao, S.K. Wu, C. Lin, C.H. Chen, Nano-precipitates in severely deformed and low-temperature aged CoCrFeMnNi high-entropy alloy studied by synchrotron small-angle X-ray scattering, Intermetallics 105 (2019) 146–152.
[31] A. Biswas, D.J. Siegel, C. Wolverton, D.N. Seidman, Precipitates in Al-Cu alloys revisited: atom-probe tomographic experiments and first-principles calculations of compositional evolution and interfacial segregation, Acta Mater. 59 (2011) 6187–6204.
[32] T.J. Konno, K. Hiraga, M. Kawasaki, Guinier-Preston (GP) zone revisited: atomic level observation by HAADF-TEM technique, Scr. Mater. 44 (2001) 2303–2307.
[33] Y. Liu, F. Teng, F.H. Cao, Z.X. Yin, Y. Jiang, S.B. Wang, P.K. Shen, Defective GP-zones and their evolution in an Al-Cu-Mg alloy during high-temperature aging, J. Alloy. Comp. 774 (2019) 988–996.
[34] Q.F. Wang, L.D. Wang, D.Y. Zhu, Z. Lin, X. Chen, B. Sheng, Age hardening behaviour of semi-solid squeeze cast A319 aluminium alloy, Mater. Werkst. 49 (2018) 1503–1509.
[35] Y.L. Wang, H.C. Jiang, Z.M. Li, D.S. Yan, D. Zhang, L.J. Rong, Two-stage double peaks ageing and its effect on stress corrosion cracking susceptibility of Al-Zn-Mg alloy, J. Mater. Sci. Technol. 34 (2018) 1250–1257.
[36] Y.L. Wang, Y.Y. Song, H.C. Jiang, Z.M. Li, D. Zhang, L.J. Rong, Variation of nanoparticle fraction and compositions in two-stage double peaks aging precipitation of Al-Zn-Mg alloy, Nanoscale Res. Lett. 13 (2018) 131.
[37] X.B. Yang, J.Z. Liu, J.H. Chen, C.Y. Wan, L. Fang, P. Liu, C.L. Wu, Relationship between the strengthening effect and the morphology of precipitates in Al-7.4Zn-1.7Mg-2.0Cu alloy, Acta Metall. Sin. 27 (2014) 1070–1077.
[38] J.M. Silcock, T.J. Heal, H.K. Hardy, Structural ageing characteristics of binary aluminium–copper alloys, J. Inst. Met. 82 (1954) 239–248.